New Journal of Physics
The open access journal at the forefront of physics

Deutsche Physikalische Gesellschaft DPG IOP Institute of Physics

PAPER • OPEN ACCESS

Volkov transform generalized projection algorithm for attosecond pulse characterization

To cite this article: P D Keathley *et al* 2016 *New J. Phys.* **18** 073009

New Journal of Physics
The open access journal at the forefront of physics

Deutsche Physikalische Gesellschaft DPG
IOP Institute of Physics

Published in partnership with: Deutsche Physikalische Gesellschaft and the Institute of Physics

OPEN ACCESS

RECEIVED
11 March 2016

REVISED
22 May 2016

ACCEPTED FOR PUBLICATION
10 June 2016

PUBLISHED
6 July 2016

PAPER

Volkov transform generalized projection algorithm for attosecond pulse characterization

P D Keathley[1], S Bhardwaj[1], J Moses[1], G Laurent[1] and F X Kärtner[1,2]

[1] Department of Electrical Engineering and Computer Science and Research Laboratory of Electronics, Massachusetts Institute of Technology, 77 Mass. Ave, Cambridge, MA 02139, USA
[2] Center for Free-Electron Laser Science, DESY and Department of Physics, University of Hamburg, Notkestraße 85, D-22607 Hamburg, Germany

E-mail: franz.kaertner@cfel.de

Keywords: attosecond pulse characterization, attosecond science, strong-field physics, attosecond metrology, ultrafast optics, frequency resolved optical gating, atomic molecular and optical physics

Abstract

An algorithm for characterizing attosecond extreme ultraviolet pulses that is not bandwidth-limited, requires no interpolation of the experimental data, and makes no approximations beyond the strong-field approximation is introduced. This approach fully incorporates the dipole transition matrix element into the retrieval process. Unlike attosecond retrieval methods such as phase retrieval by omega oscillation filtering (PROOF), or improved PROOF, it simultaneously retrieves both the attosecond and infrared (IR) pulses, without placing fundamental restrictions on the IR pulse duration, intensity or bandwidth. The new algorithm is validated both numerically and experimentally, and is also found to have practical advantages. These include an increased robustness to noise, and relaxed requirements for the size of the experimental dataset and the intensity of the streaking pulse.

1. Introduction

The state of attosecond science has progressed rapidly in the past decade, with many illuminating experiments that have explored how attosecond pulses can be used to initiate or probe electron dynamics on the attosecond time scale [1–7]. As we move forward to the next decade of attosecond science, it is of vital importance to continue in the development of both flexible and accurate techniques for characterizing the attosecond pulse itself, the backbone of all such measurements. To that end, in this article we present a new method entitled the 'Volkov transform' generalized projections algorithm (VTGPA).

The landscape of attosecond pulse retrieval techniques can be broken down into two basic approaches: generalized projections algorithms (GPA) (e.g. frequency resolved optical gating for complete retrieval of attosecond bursts (FROG-CRAB) [8, 9]), and frequency domain interferometric methods (e.g. reconstruction of attosecond beating by interference of two-photon transitions (RABBITT) [10], phase retrieval by omega oscillation filtering (PROOF) [11], or improved PROOF (iPROOF) [12]). FROG-CRAB combines the strong-field formulation of photoionization of a target in a 'strong' infrared (IR) field with the frequency resolved optical gating (FROG) technique developed for visible/IR femtosecond pulse characterization. It is commonly used as it is based on established techniques and has a sense of familiarity within the community. However, this method is limited to relatively narrow bandwidths due to the central momentum approximation (CMA), and provides no direct means of adequately incorporating the physics of the photoionization process.

The PROOF method [11] avoids the CMA, and iPROOF [12] completes a full generalization of the RABBITT technique for an arbitrary spectrum (i.e. continuum or pulse train), while incorporating physics of the photoionization process. However, both PROOF and iPROOF limit one to streaking fields that are within the perturbative intensity regime, and are restricted to streaking pulse durations that satisfy the slowly varying envelope approximation. This limits their effectiveness in experiments that require one to simultaneously

characterize an attosecond pulses along with complex, broadband electric field waveforms that clearly violate these conditions [13].

The root cause of the CMA in the FROG-CRAB technique is its reliance on the use of Fourier transforms This paper introduces a generalized projections algorithm based on a least squares (LS) minimization approach that can be used in such a way that there is no use of Fourier transforms in the retrieval process. This allows one to fit the full form of the strong-field approximation (SFA) without the need for the CMA, and provides a straightforward way to incorporate the dipole transition matrix element (DTME) into the fitting procedure. Furthermore, it does not require that the data be interpolated in the energy domain in order to satisfy constraints of a fast Fourier transform (FFT).

By decomposing the vector potential into a carrier wave and envelope, we show that the number of terms needed to fit it can be reduced significantly. Beyond reducing the computational overhead, this also improves the retrieval's robustness to noise. For an isolated pulse with a bandwidth of 100 eV, we were able to reduce the VTGPA retrieval time to less than 1.5 h on a standard desktop computer. The current state of the art method for FROG-CRAB, the least squares generalized projections algorithm (LSGPA) [9], had a faster retrieval time for the same pulse parameters (several minutes), but this was made up for in accuracy as the overall mean squared error (MSE) of the VTGPA retrieval was reduced by up to three orders of magnitude when compared to that of the LSGPA. While the integration step needed for the VTGPA is currently not as optimized as a FFT, it is shown that per iteration it converges to the solution at a faster rate than the LSGPA.

Unlike PROOF and iPROOF, this approach does not assume that the photon energy of the IR streaking pulse is well defined, nor that the field strength is sufficiently weak such that two-photon absorption of IR does not occur, making it suitable for simultaneously retrieving both the broadband attosecond pulse along with complex IR waveforms. An *in situ* characterization of both pulses simultaneously, as provided by this approach, will prove advantageous when analyzing experiments that depend equally on both pulse forms, such as in [4, 14, 15].

2. Problem overview

According to the SFA, the complex amplitude describing the transition of the ground state to a final momentum k is given by equation (1)

$$\tilde{a}(k,\tau) = -\mathrm{i}\int_{-\infty}^{\infty} \mathrm{d}t \tilde{d}_{k+A(t)} \tilde{E}_{\mathrm{X}}(t-\tau) \exp\left\{\mathrm{i}\left(I_{\mathrm{p}} t + k^2 t/2 - \int_{t}^{\infty} \mathrm{d}t' [kA(t') + A^2(t')/2]\right)\right\}. \quad (1)$$

In the expression, $\tilde{E}_{\mathrm{X}}(t)$ describes the complex electric field envelope of the extreme ultraviolet (EUV) pulse, $\tilde{d}_{k+A(t)}$ the dipole transition matrix element, I_{p} the ionization potential of the gas being ionized, $A(t)$ the vector potential due to the streaking field, given by $E_{\mathrm{L}}(t) = -\partial A/\partial t$, and τ the delay between the EUV and streaking pulses. In the expression, k is treated as a scalar as we are only concerned with those electrons going in the direction of the electron spectrometer. The same applies for $A(t)$, which we assume to be aligned in the direction of the spectrometer. The probability of measuring the electron at momentum k and delay τ is then given as $P(k,\tau) = |\tilde{a}(k,\tau)|^2$. Unless otherwise stated, atomic units are used throughout the manuscript. While it is straightforward to measure $P(k,\tau)$ directly at each delay, the difficulty in reconstructing the attosecond pulse is to develop a reliable routine for determining the phase of each momentum component.

A typical approach is to use the fact that, for a narrowband EUV pulse and non-dispersive $\tilde{d}_k$, one can make the approximation that $P(k,\tau)$ closely resembles a FROG spectrogram, given by

$$S(\omega,\tau) = \left|\int_{-\infty}^{\infty} \mathrm{d}t \tilde{E}_{\mathrm{P}}(t-\tau)\tilde{E}_{\mathrm{G}}(t)\mathrm{e}^{\mathrm{i}\omega t}\right|^2, \quad (2)$$

where $\tilde{E}_{\mathrm{P}}$ and $\tilde{E}_{\mathrm{G}}$ are complex pulse and gate functions respectively. An iterative solution can be developed to determine $\tilde{E}_{\mathrm{P}}(t)$ and $\tilde{E}_{\mathrm{G}}(t)$ from (2) with no prior knowledge of either the pulse or gate [16], and this has been utilized and extended by others for characterizing attosecond EUV pulses [8, 9]. The fundamental limitation of this approach is that, aside from the $k^2/2$ term, to conform (1) to the form of (2) it must be assumed that $k \approx k_0$, where k_0 is the central momentum of the emitted electron packet as Fourier transforms are required. This substitution explicitly defines the CMA, and it affects the accuracy of the retrieval process in two key ways for attosecond EUV pulses with large bandwidths relative to k_0. First is the inability to accurately describe the induced phase from the vector potential, and second is the inability to accurately describe dispersive regions of $\tilde{d}_{k+A(t)}$ [9], as both are inseparable functions of momentum and time.

These issues were circumvented in both PROOF and iPROOF by using a different procedure that tracks the phase and magnitude of oscillations in the spectrogram that occur at the streaking frequency. However, both of these methods assume a relatively long and weak streaking pulse such that the IR photon energy is well defined, and that the emission and streaking can be described by the absorption of one EUV photon followed by the absorption or emission of just one IR photon.

As near single-cycle infrared field transients and attosecond optical pulses are becoming available [13, 17–19], it will clearly be advantageous to use one measurement to simultaneously characterize both a complex IR pulse, which might not satisfy the above approximations, along with a broadband EUV pulse. In order to achieve this, the algorithm outlined below revisits the FROG-CRAB approach by circumventing the need for any Fourier transforms within the reconstruction.

3. Algorithm design

In order to solve for the attosecond pulse without the need of a Fourier transform, a LS minimization is performed directly in the frequency domain. A LS figure of merit, M, is defined as

$$M = \sum_{l=0}^{N_W-1} \Delta W[l] \sum_{m=0}^{N_\tau-1} \Delta\tau \, |\tilde{a}[l, m] - \tilde{a}'[l, m]|^2. \tag{3}$$

The bracket notation indicates the sampled form of the corresponding continuous function. The step size in delay is accounted for with $\Delta\tau$, and the step size in energy with ΔW. For each delay step, m, and detected photoelectron energy, l, the matrix $\tilde{a}[l, m]$ is calculated by numerically integrating equation (1)

$$\tilde{a}[l, m] = -\mathrm{i}\Delta t \sum_{n=0}^{N_E-1} \tilde{d}_{(k[l]+A[n+Lm])} \tilde{E}_X[n] \exp\{\mathrm{i}(I_p + k[l]^2/2)n\Delta t\} \times \exp\left\{-\mathrm{i}\Delta t \sum_{b=n+Lm}^{N_A-1} \Phi[l, b]\right\}, \tag{4}$$

where N_E is the number of points comprising $\tilde{E}_X[n]$, and the action-induced energy shift, $\Phi[l, n]$, is given as

$$\Phi[l, n] = k[l]A[n] + A[n]^2/2. \tag{5}$$

As with the LSGPA, the time resolution of $\tilde{E}_X[n]$ and $A[n]$ is set to be $\Delta t = \Delta\tau/L$, where L is the number of time resolution steps per delay step $\Delta\tau$, and the reader is referred to [9] for a more detailed explanation of how the delay step is implemented. While here we assume a uniform L as a function of delay for simplicity, non-uniform delay steps could easily be accounted for by making L a function of delay [9]. Also, as with LSGPA, using such a delay approach assumes no periodicity in the delay of the spectrogram. The matrix $\tilde{a}'[l, m]$ is formed by taking the $\tilde{E}_X[n]$ and $A[n]$, calculating $\tilde{a}[l, m]$, and then the measured amplitude is projected onto it. This is expressed as

$$\tilde{a}'[l, m] = \sqrt{P[l, m]} \exp\{\mathrm{i} \arg(\tilde{a}[l, m])\}. \tag{6}$$

The initial squared error in equation (3) is then simply due to any difference between the square root of the measured spectrogram, $\sqrt{P[l, m]}$, and $|\tilde{a}[l, m]|$ calculated using the current $E_X[n]$ and $A[n]$. The error is summed across all N_τ delay points and N_W energy points.

The calculation in equation (4) is more related to a discrete Fourier transform of a non-periodic function in time as opposed to a FFT. This removes the strict relationship between the energy and time sampling of an FFT, and removes the need to interpolate the measured spectrogram. To accommodate for a nonuniform energy spacing in the figure of merit calculation, the energy resolution at each l, $\Delta W[l]$, is included. The discrete integral in equation (4) is however different from a discrete Fourier transform as the outgoing state is described by a Volkov wave [20] rather than a plane wave. Thus, since we are preserving the Volkov wave basis set in this algorithm, it is called the 'Volkov transform' generalized projection algorithm. At this point, all of the components are in place to setup a minimization routine for determining $\tilde{E}_X$. We perform a LS minimization using the figure of merit by writing $\tilde{E}_X[n] = \alpha[n]\mathrm{e}^{\mathrm{i}\phi[n]}$, and solving for each term $\alpha[n]$, $\phi[n]$ such that

$$\frac{\partial M}{\partial \alpha[n]} = 0$$
$$\frac{\partial M}{\partial \phi[n]} = 0. \tag{7}$$

This leads to the following system of equations

$$0 = \mathrm{Im}\{\mathrm{e}^{\mathrm{i}\phi[c]}(\tilde{\Gamma}[c] + \tilde{\beta}[c])\}$$
$$0 = \alpha[c] \sum_{l=0}^{N_W-1} \Delta W[l] \sum_{m=0}^{N_\tau-1} \Delta\tau \, |\tilde{d}_{k[l]+A[n+Lm]}|^2 + \mathrm{Re}\{\mathrm{e}^{\mathrm{i}\phi[c]}(\tilde{\Gamma}[c] + \tilde{\beta}[c])\}, \tag{8}$$

where

$$\tilde{\Gamma}[c] = \sum_{l=0}^{N_W-1} \Delta W[l] \sum_{m=0}^{N_\tau-1} \Delta\tau \sum_{\{n|0\leqslant n<N_E, n\neq c\}} \Delta t^2 \tilde{d}_{k[l]+A[c+Lm]} \tilde{d}^*_{k[l]+A[n+Lm]} \tilde{E}^*_X[n] \times \exp\{i(I_p + k[l]^2/2)\Delta t(c-n)\} \times \exp\left\{i\Delta t \sum_{b=n+Lm}^{N_A-1} \Phi[l, b]\right\} \times \exp\left\{-i\Delta t \sum_{b=c+Lm}^{N_A-1} \Phi[l, b]\right\} \quad (9)$$

and

$$\tilde{\beta}[c] = i \sum_{l=0}^{N_W-1} \Delta W[l] \sum_{m=0}^{N_\tau-1} \Delta\tau\Delta t \tilde{d}_{k[l]+A[c+Lm]} \exp\{i(I_p + k[l]^2/2)c\Delta t\} \times \exp\left\{-i\Delta t \sum_{b=c+Lm}^{N_A-1} \Phi[l, b]\right\} \tilde{a}'^*[l, m]. \quad (10)$$

By adding both equations in (8), and manipulating to solve for $\tilde{E}_X[n] = \alpha[n]e^{i\phi[n]}$, we find that

$$\tilde{E}_X[n] = \frac{-(\tilde{\Gamma}[n] + \tilde{\beta}[n])^*}{\sum_{l=0}^{N_W-1} \Delta W[l] \sum_{m=0}^{N_\tau-1} \Delta\tau \, |\tilde{d}_{k[l]+A[n+Lm]}|^2}. \quad (11)$$

The routine for solving for $\tilde{E}_X$ starts with some initial guess for $\tilde{E}_X$ and A. From there, $\tilde{a}'[l, m]$ is formed using equations (4) and (6), and this matrix is then stored. From there, each term of $\tilde{E}_X$ is solved for sequentially using equation (11) and used to update the $\tilde{E}_X$ vector before proceeding onto the next term. In practice, the algorithm was found to work best when moving sequentially from term 0 to term $N_E - 1$, and then moving backwards from term $N_E - 1$ down to term 0 in the next run. For instance, if $\tilde{E}_X$ were to have three terms, the algorithm would solve for term 0, then 1, then 2, then 2, then 1, then 0. When moving purely in one direction, more emphasis is placed on later terms, creating an asymmetry between the left half and right half of the retrieved EUV pulse in time. This leads to a walkoff of the EUV pulse in time, causing the retrieval to break down when the pulse reaches the edge of the integration window.

After updating each term of $\tilde{E}_X$ as described above (once forwards, once backwards), one then needs to update the A vector. While $\tilde{E}_X$ can be solved using a linear LS approach, solving for $A[n]$ in this manner is not as straightforward. One could implement a nonlinear LS minimization routine, however a more direct solution exists as much more experimental information is typically known about $A[n]$. For the streaking pulse, the precise central wavelength, bandwidth, peak intensity, and, often, pulse duration are typically known to within reasonable bounds, making a bounded minimization routine possible. Rather than letting each sample in $A[n]$ be fit independently as in other routines, the vector potential can be broken down into a few key terms describing the envelope and carrier portions of the wave. The envelope, $A[n]$, can be described as a cubic spline between J points, and the carrier wave using K coefficients as $\cos(\alpha_0 + \alpha_1 t + \cdots + \alpha_{K-1}t^{K-1})$. Thus, only $J + K$ terms are used to describe $A[n]$. As an example, for a pulse with a central wavelength of 800 nm and duration of 10 fs, typically only one to two points per cycle are necessary to describe the envelope. Even if one uses up to six α terms to describe the chirp, which might be desired to fit a broadband optical field transient, for example, this gives just 14 terms to fit. It is straightforward in this case to directly minimize the figure of merit for each term, given by

$$M_A = \sum_{l=0}^{N_W-1} \Delta W[l] \sum_{m=0}^{N_\tau-1} \Delta\tau \, ||\tilde{a}[l, m]| - \sqrt{P[l, m]}|^2. \quad (12)$$

To minimize each term, Brent's method was used [21, 22]. In order to speed up the minimization, the bounds on each term were adaptively reduced as the algorithm converged. This can be further extended to synthesized waveforms, where one could create $A[n]$ by summing multiple sub-pulses, each having their own envelope and carrier components [23]. An example demonstration of an $A[n]$ calculation is shown in figure 1. An added benefit of reducing the amount of terms used to fit $A[n]$ is that less data is necessary to fit both the IR and XUV pulses. In fact, in most cases using spectrogram data from just one cycle of the streaking pulse was more than enough to get a full fit of the EUV pulse. Thus, for a full experimental trace, multiple retrievals of the EUV pulse could be performed to obtain statistics. It was found in practice that the fit for $A[n]$ converges much faster than the fit of $\tilde{E}_X$, meaning that the algorithm could be sped up further by minimizing $A[n]$ less and less often as the algorithm progresses, rather than every cycle as performed here.

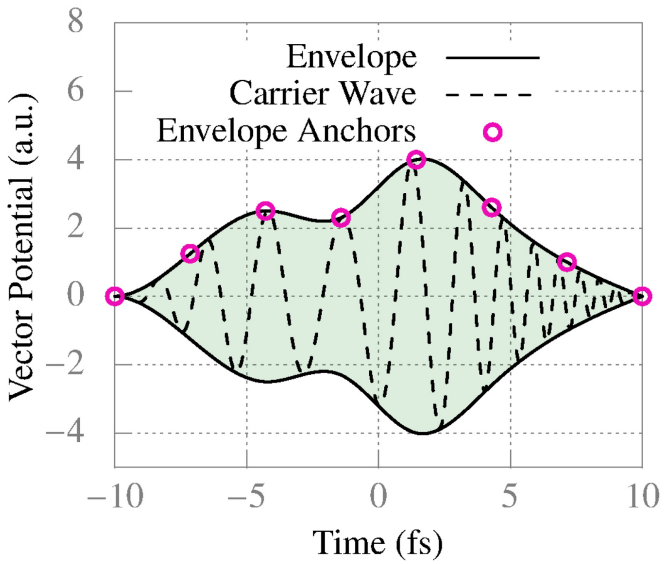

Figure 1. Plot demonstrating how the vector potential A is formed from a carrier and envelope function. The circles represent the amplitude handles used to create a spline-fit. In this plot, a fourth-order polynomial was used to represent the carrier wave underneath, making for a total of 13 terms. To fit the same function with a time resolution of 50 as using LSGPA or PCGPA would require 400 terms.

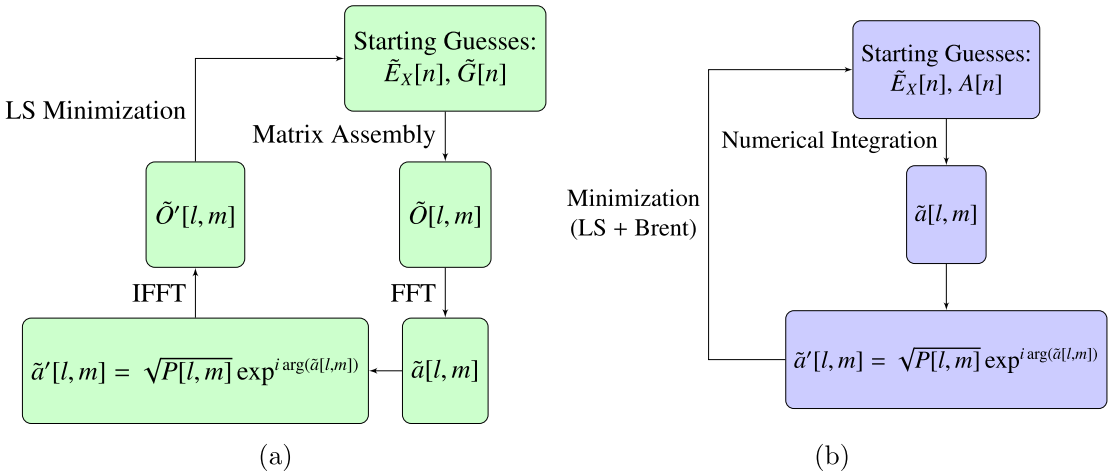

Figure 2. (a) A flowchart of the LSGPA algorithm. In LSGPA, the complex gate function, $\tilde{G}[n]$, is used to represent the phase gate created by the laser-induced action after applying the CMA. The matrix $\tilde{O}[l,\ m]$ is the time domain matrix representing the convolution of $\tilde{E}_X$ and $\tilde{G}$ before integration. (b) A flowchart of the VTGPA algorithm. The flowchart has fewer elements than other GPA approaches, but more computation is being performed in the minimization step. No FFTs are used, and the minimization is performed directly in the frequency domain.

After populating a next guess for both $\tilde{E}_X$ and A, the process is repeated until some convergence criteria are satisfied. Flowcharts summarizing both the LSGPA and VTGPA are shown in figure 2. The main achievement of VTGPA is that it requires no FFT step, leaving the SFA as the only remaining approximation. It should also be noted that, in principle, this approach should still work with other ionization models or versions of the SFA with only slight modifications so long as the expression in the integral is directly proportional to $\tilde{E}_X$.

4. Results and discussion

The VTGPA was tested and compared to LSGPA using a simulated spectrogram. The spectrogram was created using an attosecond EUV pulse having a cosine-squared profile in the energy domain with a bandwidth of 120 eV, a central energy of 80 eV, and a group delay dispersion of -2.17×10^{-3} fs^2. To this pulse, a small side-lobe was added having the same profile, but with a bandwidth of 100 eV, the same chirp, a time separation of 100 as, and roughly 1/4 peak electric field magnitude. The IR streaking pulse had a center wavelength of 800 nm,

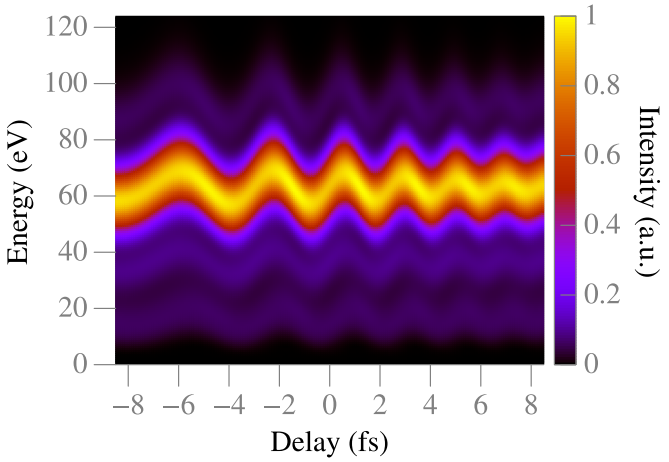

Figure 3. Simulated spectrogram used for testing the reconstruction. An attosecond EUV pulse with a cosine-squared profile in the energy domain was used. Its bandwidth was set to 120 eV with a central energy of 80 eV, and a group delay dispersion of -2.17×10^{-3} fs^2. A small side-lobe pulse was included, having the same profile, but with a bandwidth of 100 eV, the same chirp, a time separation of 100 as, and roughly 1/4 peak electric field magnitude. For the IR streaking pulse, a center wavelength of 800 nm, and a Gaussian envelope with duration of 10 fs full width at half maximum (FWHM) in intensity, a linear chirp of 25.5×10^{-3} fs^{-2}, and a peak intensity of 1×10^{12} W cm^{-2} was used. The target gas was modeled using simulation data for the DTME of Ar.

and a Gaussian envelope with duration of 10 fs full width at half maximum (FWHM) in intensity, a linear chirp of 25.5×10^{-3} fs^{-2}, and a peak intensity of 1×10^{12} W cm^{-2}. Argon was used as a target gas in the simulation. The DTME used for simulating the spectrogram was calculated using the method described in [24]. The resulting spectrogram is shown in figure 3.

Each algorithm was configured to stop after reaching a convergence criterion, which was set to be when the percent difference between the current figure of merit value, as defined by M_A, and previous figure of merit, M'_A, is less than 1×10^{-5}, i.e.

$$\frac{2(M_A - M'_A)}{M_A + M'_A} < 1 \times 10^{-5}. \tag{13}$$

A comparison of the results are shown in figure 4.

While the VTGPA result retrieves the exact attosecond pulse envelope and phase, LSGPA suffers significant error. In fact, it appears as if the LSGPA simply retrieves a near transform-limited pulse with a duration roughly half that of the actual pulse. For the streaking pulse, the LSGPA algorithm underestimates the peak field amplitude, and has the addition of extra, unphysical noise due to the differentiation step when converting from $\Phi(t)$. This is not an issue in VTGPA as the peak amplitude is fitted correctly, and there is no additional noise as it is constrained to a smooth function. With regard to the streaking intensity, it has been shown that algorithms such as the principle components generalized projection algorithm (PCGPA) and LSGPA are even less effective if the streaking intensity is reduced below 1×10^{13} W cm^{-2} for EUV pulses of such large bandwidth [11]. However, using the same EUV input pulse as above, VTGPA was tested down to a streak intensity of 1×10^{11} W cm^{-2} without any loss in accuracy (see figure 5(a)). Furthermore, for pulse trains, VTGPA successfully retrieved pulses with streaking intensities as low as 1×10^{9} W cm^{-2} (see figure 5(b)). This is advantageous for avoiding such phenomena as Stark shifts and background electron contamination from ATI during measurement.

To investigate the fundamental source of the error, the retrieval was performed on a spectrogram created using the same input pulses, only this time assuming a spectrally flat DTME. The results are shown in figure 6. With the flat DTME, the XUV pulse retrieved with the LSGPA exhibited almost identical error to that with the DTME included (shown in figure 4(a)). This indicates that the greatest source of error for the LSGPA in this particular case is the application of the CMA inside of the calculation of Φ. To verify this, we can plot the difference between the original and retrieved spectrograms for each algorithm (see figure 7). Note that there is a two order of magnitude difference between the color bar scales in figures 7(a) and (b). It is clear that for the case of the LSGPA, the greatest contribution to the error comes from locations where there is the largest ponderomotive energy shift.

To compare the computational efficiency of the two algorithms, the MSE between the square root of the retrieved and original spectrogram amplitude (i.e., $M_A/(N_W N_\tau)$) as a function of iterations is plotted in figure 8. We consider an iteration to be one complete cycle fitting all of the terms of $\tilde{E}_X$. Since in each cycle of the VTGPA algorithm we fit the terms of $\tilde{E}_X$ twice (moving forwards, then backwards), we count each cycle to be two

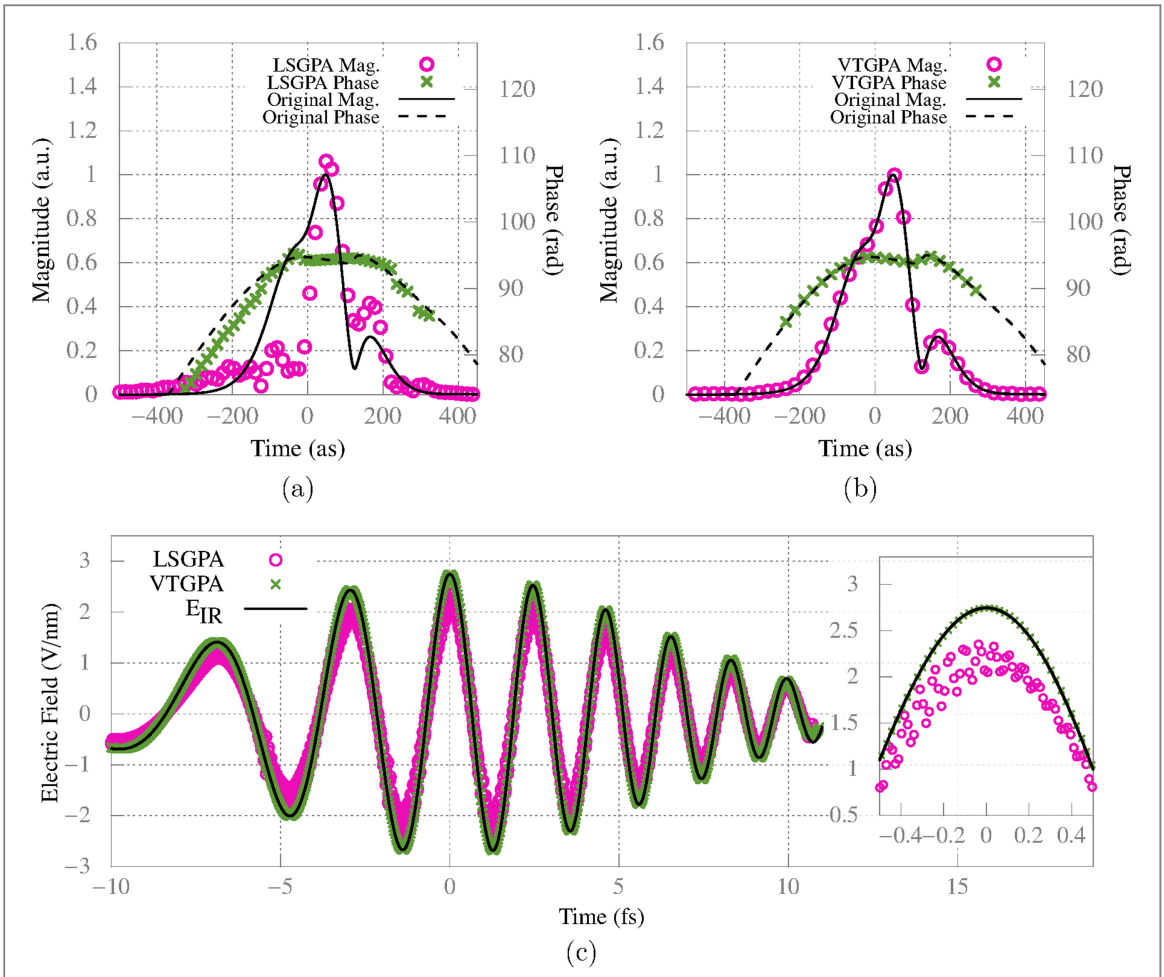

Figure 4. (a) LSGPA retrieval of $\tilde{E}_X$. As others have observed [11], the algorithm retrieves a pulse much shorter than the actual value, in this case roughly 50% of the actual FWHM. While the side lobe location is correct, the side lobe intensity is incorrectly retrieved. (b) VTGPA retrieval of $\tilde{E}_X$. (c) Comparison of the IR field retrieval using both algorithms. While LSGPA correctly retrives the shape of the IR field, the peak field strength is underestimated, as noted in [9]. Also, since it retrieves a fit to $\int_t^\infty \Phi(t')\,dt'$, not $E_{IR}(t)$ directly, it also increases the noise of the fit due to differentiation. On the other hand, the VTGPA routine forces $A(t)$, and thus $E_{IR}(t)$, to be described by a smooth function which does not introduce extra noise into the fit, and the field magnitude is correctly retrieved. Inset shows a zoom near the peak electric field at 0 fs.

iterations here. The VTGPA achieved an MSE three orders of magnitude less than that of the LSGPA. Furthermore, it converged at a faster rate per iteration, making the integration step the only bottleneck in terms of the absolute time spent per retrieval.

While it is difficult to make comparisons in terms of speed, as many factors contribute such as the exact size of the spectrogram and desired resolution, in general, for the same number of iterations the LSGPA computes faster than the VTGPA in our implementations. The major limiting factor preventing the VTGPA from computing as quickly as the LSGPA is the fact that the integration step in the minimization procedure was not as optimized as the FFT procedure used for the LSGPA. With a proper selection of fit parameters, we were able to achieve the same level of accuracy shown within 1.5 h on a standard desktop computer using the VTGPA with the EUV pulse having a 100 eV bandwidth. Of course, this time improves with decreasing bandwidth. For instance, a pulse with a bandwidth of 30–40 eV can be retrieved within 15–20 min using our current implementation. This makes the VTGPA an attractive choice even for narrower bandwidths in regions where the DTME is highly dispersive, such as at low energies [24]. While preliminary, we have also begun testing methods that ignore samples in the EUV pulse that are not contributing significantly to the fit, which have shown speed enhancements up to 33%.

Any experimental measurement will of course have noise, and to give a proper comparison of each algorithm's performance under more realistic conditions, Poisson noise was added to the spectrogram in figure 3. The magnitude of the noise resulted in the spectrogram having a signal-to-noise ratio of SNR $\approx$ 7.7, where the SNR is defined as

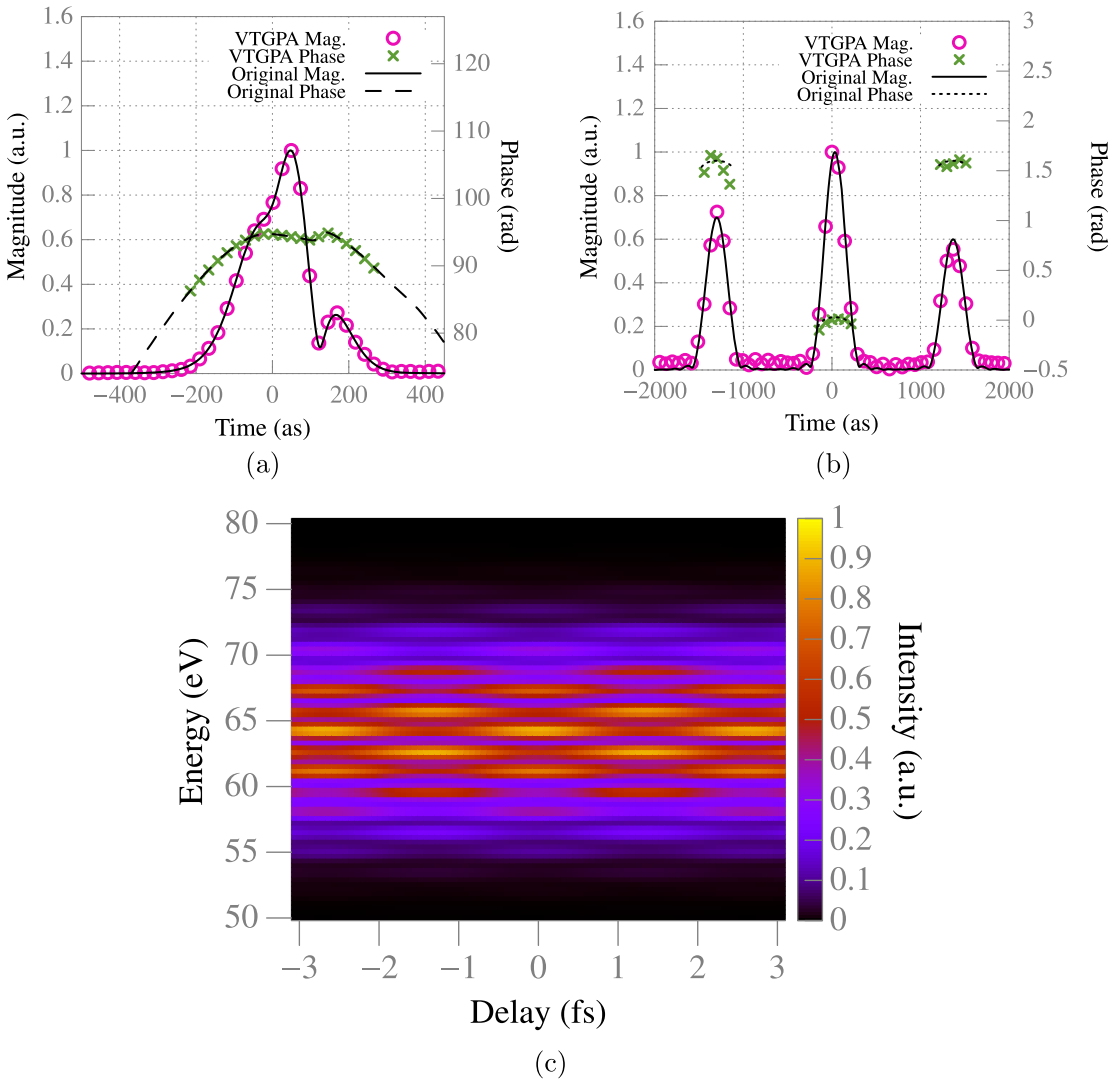

Figure 5. Demonstration of VTGPA performance with low streaking intensity. (a) Retrieval using same parameters as described for results shown in figure 4, but with a reduced peak streaking intensity of 1×10^{11} W cm^{-2}. (b) Retrieval of a pulse train exhibiting both even and odd harmonics similar to what is presented in the experimental results. The attosecond EUV pulses each have a cosine-squared profile in the energy domain with a 30 eV bandwidth. In the time domain, the outer pulses have a net phase difference of $\pi/2$ rad relative to the center pulse. (c) The spectrogram of the pulse train used for the retrieval shown in (b). The streaking pulse has a transform-limited Gaussian profile in time with a duration 15 fs FWHM, and a peak intensity of 1×10^{9} W cm^{-2}.

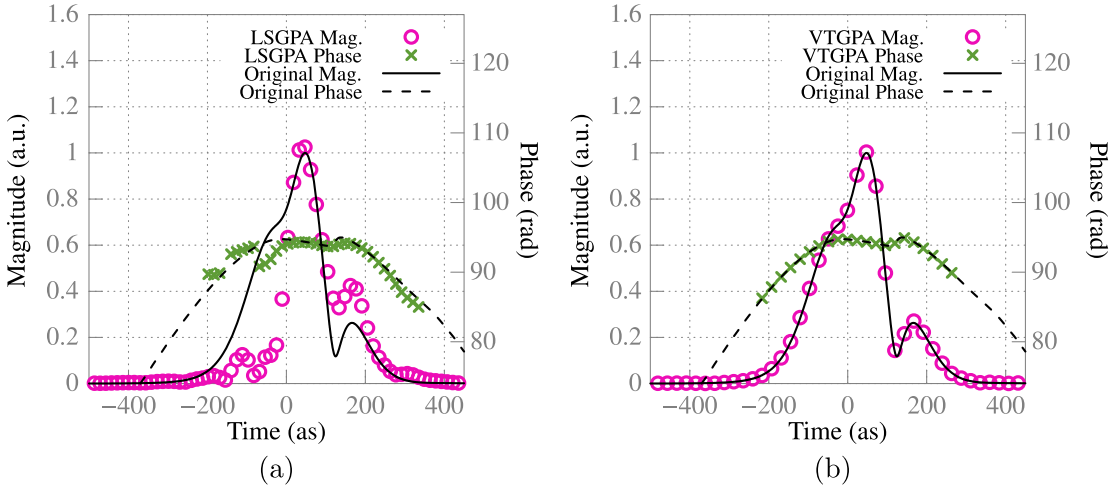

Figure 6. Retrieval results using a spectrally flat DTME. (a) LSGPA retrieval of $\tilde{E}_X$. (b) VTGPA retrieval of $\tilde{E}_X$.

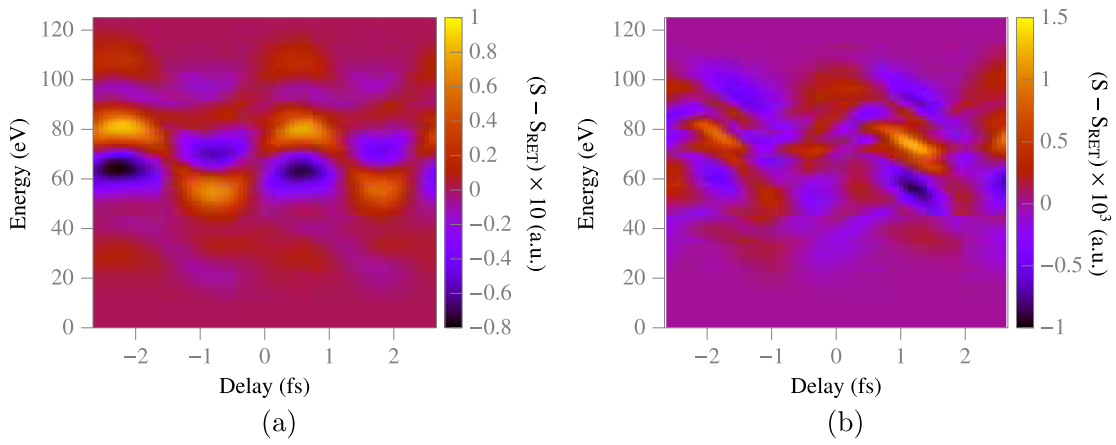

Figure 7. Pseudocolor plots of the difference between the original and retrieved spectrograms for the case of a flat DTME when using (a) the LSGPA and (b) the VTGPA. In (a) the error is dominated by regions of the plot that correspond to greatest ponderomotive energy shift, consistent with error due to the CMA. Note that the colorbar scales are different by two orders of magnitude.

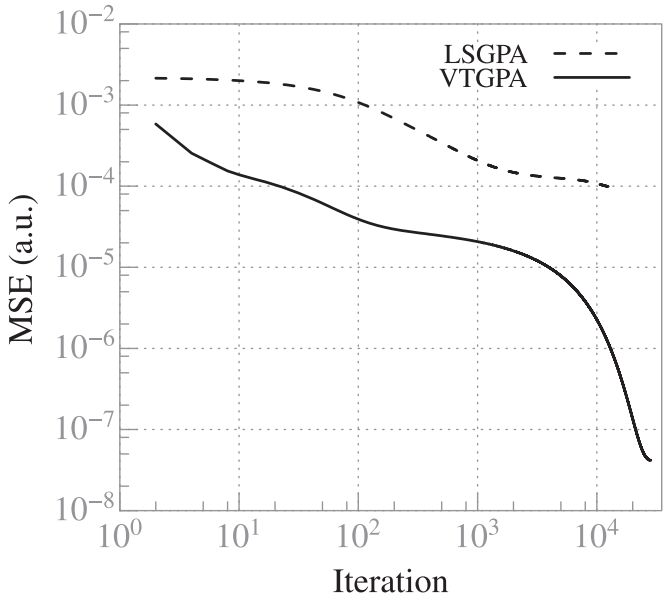

Figure 8. Log–log plot of the mean squared error between the retrieved and original spectrograms versus the number of iterations for both the LSGPA (dashed) and VTGPA (solid).

$$\mathrm{SNR} = \frac{\sqrt{\sum_{l,m} P[l,\ m]^2}}{\sqrt{\sum_{l,m} N[l,\ m]^2}} \tag{14}$$

and $N[l,\ m]$ is the noise amplitude at each pixel location. The resultant spectrogram after adding noise is shown in figure 9, and the results of the two retrieval algorithms are shown in figure 10.

The LSGPA algorithm fared significantly worse in the presence of noise, again retrieving a main pulse shorter than the actual duration, with an added pedestal at earlier times that extends out to roughly twice the width of the actual pulse. Furthermore, while it does retrieve a side lobe after the main pulse, the side lobe's intensity and location are retrieved incorrectly. On the other hand, the VTGPA algorithm retrieved a pulse that matches much better to the original pulse shape, having a duration that is only slightly shorter. More importantly, the side lobe location and intensity are both accurately retrieved. It should be noted here that for the VTGPA retrieval shown in figures 4(b) and 6(b), it was only necessary to use a region of the spectrogram near the center spanning only a single cycle of the streaking pulse to fit the EUV pulse, while in the presence of noise this was extended to roughly four cycles to make the system more overdetermined and improve the fit. However, in all cases, the LSGPA was performed across the entire spectrogram.

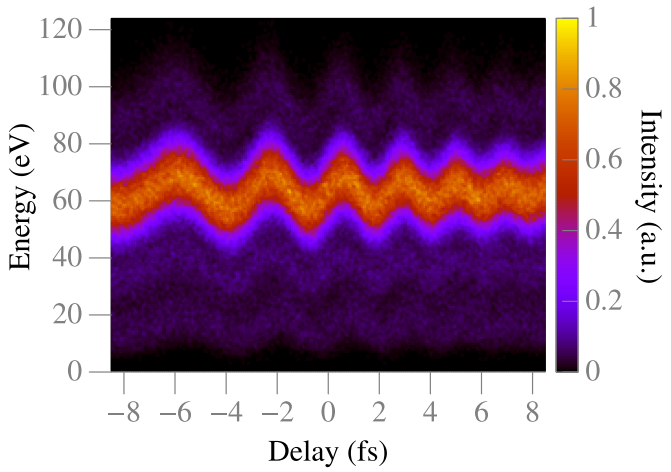

Figure 9. The spectrogram after the addition of Poisson noise.

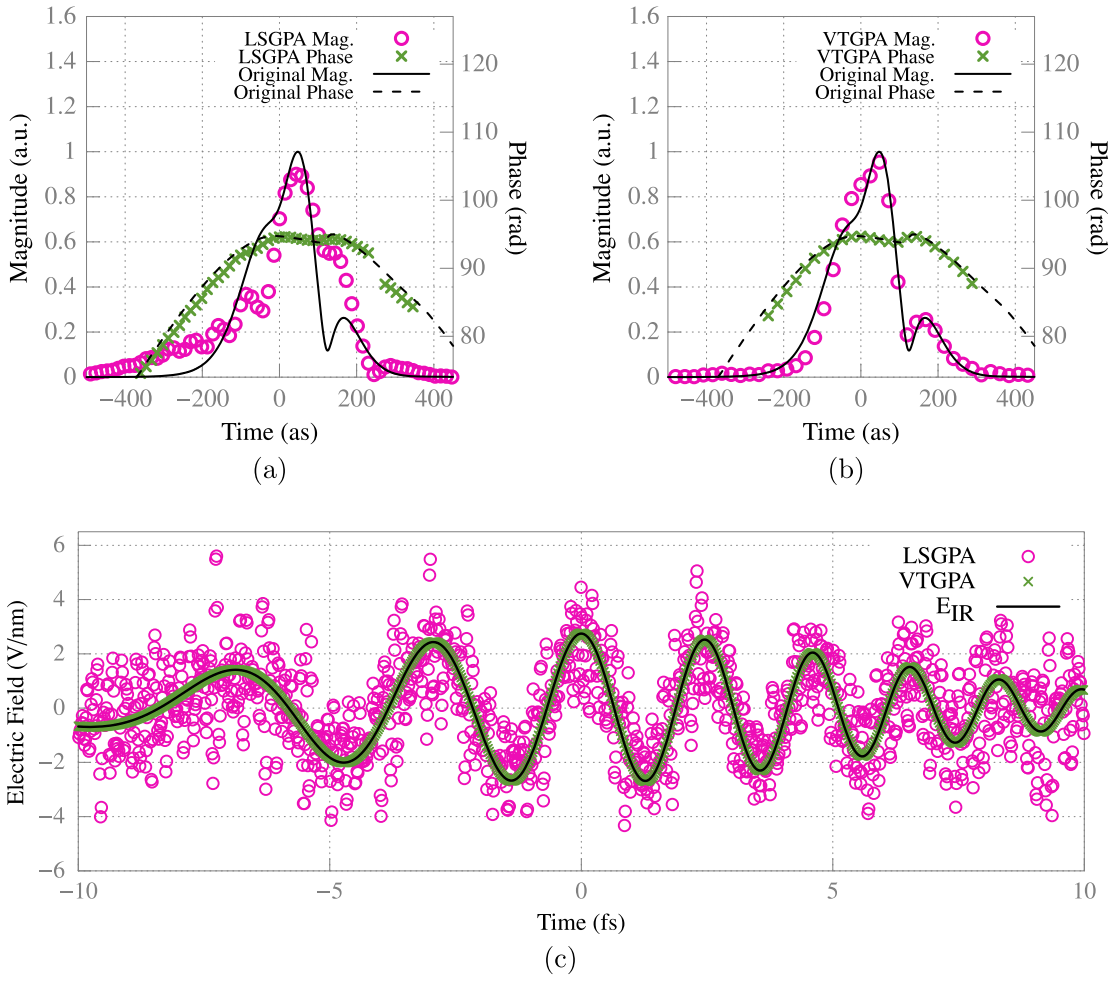

Figure 10. (a) The LSGPA results after the addition of Poisson noise to the spectrogram. Again the pulse duration is underestimated, but now there is the development of a long pedestal, and neither the side lobe location and intensity are retrieved accurately. (b) The VTGPA results. While there is a slight amount of error introduced, the overall pulse shape, duration and side lobe are all quite accurately retrieved. (c) Comparison of retrieval results for the IR streaking pulse using both algorithms. There is no loss of accuracy for the VTGPA routine, while the LSGPA results suffers considerably due to the differentiation step.

The streaking pulse retrieval results shown in figure 10(c) demonstrate how the noise in the LSGPA result gets further magnified due to the differentiation step necessary for converting the streaking phase result into the streaking electric field waveform. Again, the VTGPA algorithm does not suffer from this issue as it is fitting a

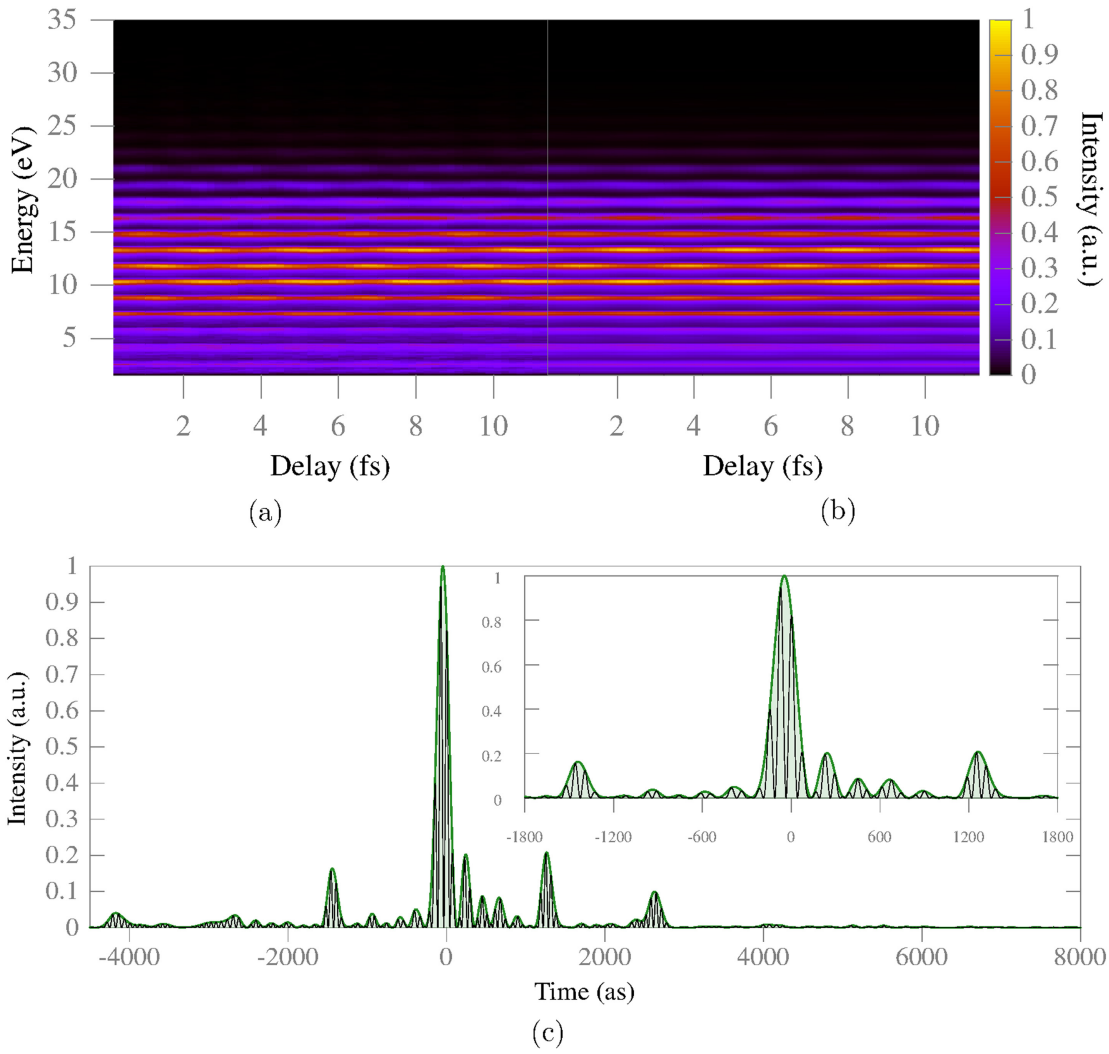

Figure 11. (a) The experimentally measured spectrogram. (b) The fitted spectrogram using VTGPA, accounting here for both the dipole transition matrix element and the transfer function of the TOF spectrometer to properly match the measured spectrogram in (a). (c) Retrieved XUV pulse intensity profile showing both the instantaneous field intensity, $(\mathrm{Re}(\tilde{E}_X))^2$, and envelope intensity, $|\tilde{E}_X|^2$. The inset shows a zoom around the largest peak and first two side-lobes. A carrier wave has been added with an arbitrary absolute phase offset for visual reference.

smooth envelope and carrier function that is not allowed to have unphysical jumps in electric field from one time sample to the next.

One final point of interest is the effect of a drift in carrier envelope phase (CEP) throughout a measurement. Until this point, it has been assumed that this drift is negligible, and our simulations show that for IR streaking pulses having a Gaussian profile in time and a duration of 5 fs FWHM, a CEP drift of 300 mrad has negligible consequence on the attosecond pulse and IR retrieval. However, for these simulations it was assumed that the attosecond EUV pulse does not change as a function of CEP drift. A thorough study of potential CEP effects, while beyond the scope of this paper, is warranted given that attosecond pulse generation and characterization experience an increased sensitivity to it when driven with few-cycle field transients.

5. Experimental validation

To experimentally validate the VTGPA, we chose to reconstruct a measured spectrogram with similar characteristics to the one tested in [12] to show that its retrieval results are consistent with expectations. The high-harmonic generation (HHG) was generated using a commercial, 800 nm pulsed laser system with a pulse duration of 35 fs and peak pulse energy of 5 mJ. The pulse was split into two arms, one for driving the HHG process, the other for streaking the photoelectrons in a second gas jet. In the drive arm, the beam was focused into a glass capillary filled with Ar gas using a curved mirror with a focal length of 25 cm, achieving peak

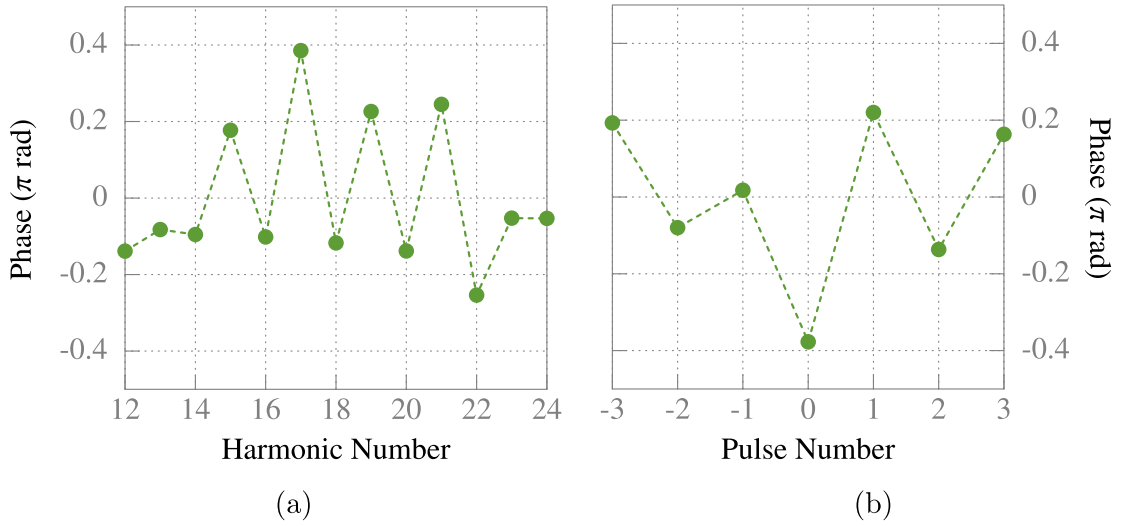

Figure 12. (a) The retrieved phase (to within an arbitrary constant) for each harmonic throughout the HHG plateau in the energy domain, and (b) at the center of each pulse in the time domain.

intensities on the order of 1×10^{14} to 1×10^{15} W cm^{-2}. A 200 μm-thick beta barium borate (BBO) crystal was placed before the curved mirror to generate the second harmonic of the 800 nm light, resulting in the generation of both odd and even harmonics. Furthermore, a half-waveplate was used before the BBO to slightly detune the polarization of the input pulse relative to the BBO crystal. Input pulse energy, beam aperture size and the half-waveplate angle were tuned for optimum even-harmonic flux. After the capillary, the IR pulse was removed and the EUV pulse spectrally filtered using a 500 nm thick, suspended Al foil. The EUV pulse was focused into the target region, a second Ar gas jet, in front of a time-of-flight (TOF) electron spectrometer using an Au coated toroidal mirror.

The streaking pulse was sent through a piezo-controlled delay line, followed by an iris and a focusing lens. The EUV and streaking beams were recombined using a drilled mirror having a roughly 2 mm hole aperture. The intensity of the streaking beam was controlled by adjusting the opening size of the iris in the streaking arm. In this case, a relatively weak streaking intensity was used, having a peak intensity of just 1.6×10^{9} W cm^{-2} according to the VTGPA fit. The electron spectra were collected using the TOF electron spectrometer. In order to calibrate the electron spectra, a Rowland-circle EUV spectrometer was used to simultaneously measure the EUV spectrum with the streaking beam blocked. The electron energy was calibrated by matching harmonic peak locations in the EUV and TOF spectra. The EUV spectrum was used in conjunction with the DTME of Ar to calibrate the TOF spectrometer's transfer function as a function of energy. The measured streaking spectrogram and fit results are combined in figure 11.

The spectrogram retrieved by the VTGPA matches very well with the measured spectrogram. As with the results reported in [12], the attosecond pulse train has contributions from each half-cycle. The even harmonics thus arise mostly due to a non-π phase shift between each EUV emission in time, which breaks the anti-symmetry necessary for the generation of only odd harmonics. The fact that the phase shift between consecutive harmonics in the plateau region is close to $\pi/2$ also explains why the beat notes generated there form the observed checkerboard-like pattern (i.e., the beat note maximum of each harmonic is lined up with the beat note minimum of adjacent harmonics). As discussed briefly in [25], an infinite pulse train with identical pulse envelopes, but an alternating phase of Θ will have harmonics having complex amplitude given by

$$\tilde{d}_N = \tilde{F}_N\{1 + (-1)^N e^{i\Theta}\}, \tag{15}$$

where $\tilde{F}_N$ is a complex constant depending on the harmonic number N, and the phase offset from one half-cycle to the next is given by Θ. For example, single-color HHG yields odd harmonics since $\Theta = \pi$. However, even a very mild second harmonic breaks this relationship, whether aligned purely parallel, orthogonal, or a mixture of both, as in our experimental arrangement. It is worth noting that a phase shift of $\Theta \approx \pi/2$ in the action phase alone is achievable with a perpendicular second harmonic component of just 0.25% of a fundamental intensity of 4×10^{14} W cm^{-2} according to the semiclassical three-step model. While our experimental conditions are not this ideal, with both a stronger parallel and slight perpendicular components to the second harmonic and a non-infinite series of non-identical EUV pulses, it is clear that such phases are easily attainable with second

harmonic fields that would not strongly influence the ionization rate and recombination energy of harmonics in subsequent half-cycles. The experimentally retrieved phase shifts between harmonics in both the time and frequency domain are shown in figure 12 for comparison.

6. Conclusion

A new algorithm, entitled 'Volkov transform' generalized projections algorithm, has been introduced. This method fully accounts for the complex action phase and DTME of the ionization process as dictated by the SFA without any further approximations. Furthermore, it has been compared with a current state of the art algorithm for FROG-CRAB, the LSGPA. We clearly demonstrate that the VTGPA is not susceptible to errors introduced by the CMA, is more robust to noise, and can easily incorporate the target atom's DTME. When compared directly to the LSGPA, the MSE between retrieved and simulated spectrograms of the VTGPA was reduced by over three orders of magnitude, and converged faster to the solution per-iteration. Due to the nature of how the minimization routine is performed, there is no need to interpolate the experimental data as a nonuniform sampling of the spectrogram in energy is allowed. In all other respects, it has the advantage of any FROG-CRAB algorithm in that it does not place any strong limitations on the IR streaking field, making it useful as an *in situ* characterization tool for both a complex IR field and attosecond EUV pulse.

Since VTGPA is able to accurately retrieve attosecond EUV pulses with very low peak streaking intensities, tested down to 1×10^{11} W cm^{-2} for an isolated pulse with ~100 eV bandwidth centered at 80 eV and 1×10^{9} W cm^{-2} for a pulse train with ~30 eV bandwidth, interfering processes such as ATI and Stark shifting can be avoided. Also, at these intensities it will provide a tool for investigating and comparing results with methods such as iPROOF, to gain a better understanding of both the perturbation theory and SFA and improve theoretical methods for approximating the complex DTMEs used in the SFA.

One area of future work will be directed towards optimizing the integration step in the algorithm for speed, perhaps using techniques that have already been employed in FFT algorithms. Another area of future work will investigate whether the concept of partial coherence can be incorporated into the retrieval process, as has already been done for the PCGPA routine [26]. The inclusion of partial coherence into any realistic retrieval routine seems an absolute necessity given the uncertainty involved with any precision measurement of this kind. While the VTGPA was presented here in the context of attosecond EUV pulse retrieval, it is felt that the overall approach should find further application in other strong-field physics studies with slight modifications.

Acknowledgments

This work was supported by the United States Air Force Office of Scientific Research (AFOSR) through grants FA9550-12-1-0080 and FA9550-12-1-0499, the Center for Free-Electron Laser Science at DESY and the excellence cluster 'The Hamburg Centre for Ultrafast Imaging-Structure, Dynamics and Control of Matter at the Atomic Scale' of the Deutsche Forschungsgemeinschaft. P D Keathley received support from the Department of Defense (DoD) through the National Defense Science & Engineering Graduate Fellowship (NDSEG) Program. The authors would also like to thank Oliver Mücke for carefully reading the manuscript and providing excellent feedback, and Alexander Sell for assistance when creating the attosecond characterization apparatus.

References

[1] Schultze M *et al* 2010 *Science* **328** 1658–62
[2] Johnsson P *et al* 2005 *Phys. Rev. Lett.* **95** 013001
[3] Cavalieri A L *et al* 2007 *Nature* **449** 1029–32
[4] Goulielmakis E *et al* 2010 *Nature* **466** 739–43
[5] Chini M, Wang X, Cheng Y, Wu Y, Zhao D, Telnov D A, Chu S I and Chang Z 2013 *Sci. Rep.* **3** 1105
[6] Swoboda M *et al* 2009 *Phys. Rev. Lett.* **103** 123005
[7] Ranitovic P, Tong X, Hogle C, Zhou X, Liu Y, Toshima N, Murnane M and Kapteyn H 2011 *Phys. Rev. Lett.* **106** 193008
[8] Mairesse Y and Quere F 2005 *Phys. Rev.* A **71** 011401
[9] Gagnon J, Goulielmakis E and Yakovlev V 2008 *Appl. Phys.* B **92** 25–32
[10] Paul P M, Toma E S, Breger P, Mullot G, Auge F, Balcou P, Muller H G and Agostini P 2001 *Science* **292** 1689–92
[11] Chini M, Gilbertson S, Khan S D and Chang Z 2010 *Opt. Express* **18** 13006–16
[12] Laurent G, Cao W, Ben-Itzhak I and Cocke C L 2013 *Opt. Express* **21** 16914–27
[13] Wirth A *et al* 2011 *Science* **334** 195–200
[14] Luu T T, Garg M, Kruchinin S Y, Moulet A, Hassan M T and Goulielmakis E 2015 *Nature* **521** 498–502
[15] Okell W A *et al* 2015 *Optica* **2** 383–7
[16] Kane D 1999 *IEEE J. Quantum Electron.* **35** 421–31
[17] Huang S W *et al* 2011 *Nat. Photon.* **5** 475–9

[18] Goulielmakis E et al 2008 Science 320 1614–7
[19] Hassan M T et al 2016 Nature 530 66–70
[20] Boca M 2011 J. Phys. A: Math. Theor. 44 445303
[21] Burkardt J and Brent R 2011 BRENT available at (http://people.sc.fsu.edu/~jburkardt/cpp_src/brent/brent.html)
[22] Brent R P 2013 Algorithms for Minimization Without Derivatives (Mineola, NY: Dover)
[23] Manzoni C, Mücke O D, Cirmi G, Fang S, Moses J, Huang S W, Hong K H, Cerullo G and Kärtner F X 2015 Laser Photon. Rev. 9 129–71
[24] Bhardwaj S, Son S K, Hong K H, Lai C J, Kärtner F X and Santra R 2013 Phys. Rev. A 88 05340
[25] Zuo T, Bandrauk A D, Ivanov M and Corkum P B 1995 Phys. Rev. A 51 3991–8
[26] Bourassin-Bouchet C and Couprie M E 2015 Nat. Commun. 6 6465